Nano Research
2020, 13(12): 3315–3320

ISSN 1998-0124 CN 11-5974/O4
https://doi.org/10.1007/s12274-020-3009-0

Research Article

Defect engineering on carbon black for accelerated Li–S chemistry

Wenlong Cai[1], Yingze Song[2] (✉), Yuting Fang[1], Weiwei Wang[1], Songlin Yu[2], Huaisheng Ao[1], Yongchun Zhu[1] (✉), and Yitai Qian[1]

[1] *Hefei National Laboratory for Physical Sciences at Microscale and Department of Chemistry, University of Science and Technology of China, Hefei 230026, China*
[2] *State Key Laboratory of Environment-Friendly Energy Materials, School of Materials Science and Engineering, Southwest University of Science and Technology, Mianyang 621010, China*

Received: 9 May 2020 / **Revised:** 23 July 2020 / **Accepted:** 26 July 2020

ABSTRACT

Rationally designing sulfur hosts with the functions of confining lithium polysulfides (LiPSs) and promoting sulfur reaction kinetics is critically important to the real implementation of lithium–sulfur (Li–S) batteries. Herein, the defect-rich carbon black (CB) as sulfur host was successfully constructed through a rationally regulated defect engineering. Thus-obtained defect-rich CB can act as an active electrocatalyst to enable the sulfur redox reaction kinetics, which could be regarded as effective inhibitor to alleviate the LiPS shuttle. As expected, the cathode consisting of sulfur and defect-rich CB presents a high rate capacity of 783.8 mA·h·g^{-1} at 4 C and a low capacity decay of only 0.07% per cycle at 2 C over 500 cycles, showing favorable electrochemical performances. The strategy in this investigation paves a promising way to the design of active electrocatalysts for realizing commercially viable Li–S batteries.

KEYWORDS

Li–S chemistry, defect engineering, carbon black, sulfur reaction kinetics

1 Introduction

Owing to the overwhelming theoretical capacity (1,672 mA·h·g^{-1}), high energy density (2,600 W·h·kg^{-1}), and low cost of sulfur, lithium–sulfur (Li–S) batteries have been regarded as one of the most promising next-generation energy storage devices [1–5]. However, the practical application of Li–S batteries have been impeded by a multitude of issues: (i) the noticeable volume variation (80%) during the continuous and repetitive transformation between sulfur and lithium sulfide; (ii) the low utilization of active materials due to the poor electronic/ionic conductivity; (iii) the notorious shutting effect of soluble lithium polysulfides (LiPSs) between the electrodes; (iv) the resultant side reactions at lithium anode side [6–10].

In recent years, extensive efforts have been devoted to addressing the above-mentioned problems for facilitating the commercialization of Li–S batteries [11–14]. Of the many alternatives, optimizing sulfur electrochemical process has been confirmed as an effective strategy to mitigate the shuttle phenomenon [15–18]. Carbonaceous materials, such as porous carbon [19], graphene [20], and carbon nanotube [21], were used at the earliest to confine LiPSs by physical adsorption. Nevertheless, such weak van der Waals affinity is insufficient to stabilize LiPSs. In this case, polar groups were introduced into carbon host, resulting in the strong polar–polar interaction with LiPSs [22–24].

Thus far, wide investigations reveal that the polar hosts should present the functions of both confining the soluble LiPSs within the cathode and promoting the sulfur redox reaction kinetics, keeping the cathode surface from infaust LiPS flooding which is caused by sluggish redox kinetics. For the past few years, a variety of hosts with good polarity and excellent conductivity show satisfied catalytic effect on LiPS conversion. Furthermore, the materials with rich defects, such as oxygen and sulfur vacancies, exhibit favorable electrocatalytic activity on the sulfur redox reaction. Carbonaceous materials act as hosts or conductive agents in the electrodes due to their excellent conductivity and chemistry stability. The recent studies disclosed that the electrocatalytic activities of heteroatom-doped carbon materials originate from activating carbon π electrons by breaking the integrity of π conjugation. Along this line, it is rational to deem that the intrinsic/induced defects in sp^2 carbon with broken π conjugation benefit to enhance the electrocatalytic activities [25–27].

Herein, defect engineering was implemented on carbon black (CB) with the assistance of rationally regulated wet-chemistry approach. Our investigation results show that the number of defects on CB can be effectively introduced by optimizing the usage of H_2O_2. As such, the thus-derived defect-rich CB can afford high electrocatalysis activity to promote kinetic conversion of the anchored LiPSs to final solid Li_2S in a working Li–S battery, so as to inhibit the shuttle effect of LiPSs. Therefore, the cathode consisting of sulfur and defect-rich CB delivers a high rate capacity of 783.8 mA·h·g^{-1} at 4 C and a low capacity decay of 0.07% per cycle at 2 C over 500 cycles.

Address correspondence to Yingze Song, yzsong@swust.edu.cn; Yongchun Zhu, ychzhu@ustc.edu.cn

TSINGHUA UNIVERSITY PRESS Springer

2 Experimental

2.1 Material preparations

2.1.1 *Synthesis of defective carbon black*

200 mg of commercial carbon black was dispersed into the 100 mL mixed solution of H_2O and ethanol with a volume ratio of 1:1 under ultra-sonication for 60 min. Then 0.5, 1, and 2 mL of H_2O_2 was added into the resulting black suspension, respectively. After magnetic stirring for 15 min, the suspensions were transferred into 500 mL of Teflon sealed autoclaves and heated at 200 °C for 6 h, respectively. After cooling down, the final black solid products were obtained by filtering the suspensions, followed by vacuum drying at 50 °C for 12 h, and denoted as CB-1, CB-2, and CB-3, respectively.

2.1.2 *Preparation of sulfur cathodes*

The homogeneous mixture of CB (or CB-1, CB-2, and CB-3) and sublimed sulfur at a mass ratio of 1:2 was sealed in a quartz tube and heated at 155 °C for 24 h. Then 90 wt.% above mixture and 10 wt.% poly (vinylidene fluoride) (PVDF) were milled in N-methyl pyrrolidone (NMP) to form a homogeneous slurry, which was casted on an Al foil and then dried at 60 °C for overnight in a vacuum. The electrodes were punched with a diameter of 13.0 mm and areal loading of ~ 1.5 $mg\cdot cm^{-2}$, which were denoted as S/CB, S/CB-1, S/CB-2, and S/CB-3, respectively.

2.2 Material characterizations

The morphologies of the samples were performed by scanning electron microscopy (SEM) (FEOL-JSM-6700F). The specific surface areas of particles were measured by Brunauer–Emmett–Teller (BET) analysis of the N_2 adsorption–desorption isotherms. X-ray photoelectron spectra (XPS) were performed by Thermo ESCALAB 250 analyzer (Al Kα radiation, $h\nu$ = 1,486.6 eV). Raman spectra were acquired by using a micro-Raman system with a 532 nm excitation laser (HORIBA LabRAM HR). Electron paramagnetic resonance (EPR) measurement (JESFA200) was carried out at room temperature with a microwave frequency of 9,084.034 Hz and the microwave power of 20 mW.

2.3 Theoretical calculations

Density functional theory (DFT) was performed by using the projector-augmented wave (PAW) method [28]. The exchange-correlation function is treated by employing the generalized gradient approximation (GGA) of Perdew–Burke–Ernzerhof (PBE) function [29]. The energy for plane-wave basis was set at 500 eV for optimizing calculations of atoms and cell optimization. The vacuum spacing in a direction perpendicular to the plane of the structure is at least 13 Å. A 3×3×1 Monkhorst-Pack *k*-point was used for both geometry optimization and electronic structure calculation of carbon surface. The DFT-D3 empirical correction was used to depict long-range van der Waals interactions. The structure with Li_2S_x molecular structures has been established. And the adsorption energy (E_{ads}) of a Li_2S_x was defined as

$$E_{ads} = E_{A/Li_2S_x} - E_{Li_2S_x} - E_A \tag{1}$$

where E_{A/Li_2S_x}, $E_{Li_2S_x}$, and E_A are the energy of structure with Li_2S_x adsorbed, Li_2S_x, and structure in the gas phase, respectively.

2.4 Electrochemical measurements

2.4.1 *Li_2S nucleation tests*

The active CB (CB-1 or CB-2, CB-3) was dispersed into ethanol and subsequently dropped onto commercial carbon paper (CP) with a diameter of 13 mm. The Li_2S_8 electrolyte was prepared by dissolving sulfur and lithium sulfide into a tetraglyme solvent with a molar ratio of 7:1. The concentration of Li_2S_8 electrolyte was 2.0 $mol\cdot L^{-1}$ [sulfur]. Then the CP-CB (CP-CB-1 or CP-CB-2, CP-CB-3) as the cathode and lithium foil as anode were assembled into a coin-typed cell (CR2016) with 20 μL of Li_2S_8 electrolyte as catholyte and 20 μL of lithium bis((trifluoromethyl)sulfonyl)azanide (LiTFSI) (1.0 $mol\cdot L^{-1}$) without Li_2S_8 as anolyte. The assembled cells were first galvanostatically discharged at 0.112 mA to 2.06 V and then potentiostatically discharged at 2.05 V for Li_2S nucleation and growth. The potentiostatic discharge was terminated when the current was below 10^{-5} A.

2.4.2 *Electrochemical measurements*

All the coin-typed cells (CR2016) were assembled in the Ar-filled glovebox, where sulfur electrode worked as cathode, lithium foil served as anode, and commercial Celgard 2400 was applied as membrane. The electrolyte was 1 $mol\cdot L^{-1}$ LiTFSI and 1 wt.% in 1:1 (*v*/*v*) 1,3-dioxolane (DOL)/1,2-dimethoxyethane (DME) mixed solvent, and the electrolyte/sulfur was controlled at 20 mL per gram sulfur for all batteries. The galvanostatic charge/discharge performances were tested within the voltage range of 1.8–2.6 V (Li/Li^+). Cyclic voltammetry (CV) curves were recorded by a CHI660E electrochemical work station (Chinstruments, China) at a scan rate of 0.1 $mV\cdot s^{-1}$. Electrochemical impedance spectroscopy (EIS) measurements were also conducted by a CHI660E electrochemical work station from 0.01 Hz to 100 kHz with an amplitude of 5 mV.

3 Results and discussion

To construct defect-rich carbon black for affording a favorable electrocatalytic effect, wet-chemistry approach is advised through the delicate usage control of H_2O_2. Such route is versatile enough to adjust the defect on CB, benefiting to optimizing the Li–S systems. The SEM images display that all the defective CB products well preserve the sphere-shaped morphology and size (~ 50 nm) of untreated CB (Fig. S1 in the Electronic Supplementary Material (ESM)). Figure S2 in the ESM reveals that the BET surface areas of CB, CB-1, CB-2, and CB-3 are 1,327.6, 1,234.1, 1,205.6, and 1,269.8 $m^2\cdot g^{-1}$, respectively, implying the abundant sites for accommodating sulfur and the same physical adsorption ability towards LiPSs. To deeply verify the existence of carbon vacancies, Raman spectroscopy was further conducted, which acts as an efficient tool to reveal the surface electronic properties of carbon materials. As shown in Fig. 1(a), the two main

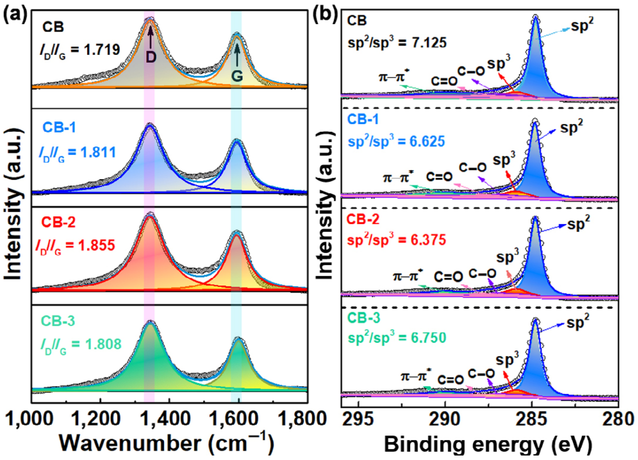

Figure 1 (a) Raman and (b) XPS C1s spectra of CB, CB-1, CB-2, and CB-3.

peaks centered at 1,590 and 1,350 cm^{-1} can be assigned to the characteristic signals for carbon materials (G and D bands) [30, 31]. The I_D/I_G intensity ratio indicates the defect information of carbon materials. After hydrothermal treatment with different usages of H_2O_2, the I_D/I_G values of CB-1, CB-2, and CB-3 are 1.811, 1.855, and 1.808, respectively, which are all higher than that of pristine CB (1.709), indicating the formation of vacancies in CB by our defect engineering. It should be noted that high usage of H_2O_2 is favorable for generating more holes and edges, resulting in the deposition of abundant defect sites on CB. However, the excessive H_2O_2 may cause the surface reconstruction, thus leading to the formation of another ordered structure and resulting in decrease of I_D/I_G intensity ratio. XPS was also performed to analyze the chemical compositions of different carbon materials. Figure S3 in the ESM reveals that all the carbon materials show only carbon element, indicating no other foreign elements was introduced. Then, the C1s spectrum deconvolution analysis was conducted for different samples. As depicted in Fig. 1(b), all the C1s peaks can be split into five peaks at 284.76, 285.93, 286.95, 287.72, and 289.98 eV, which are attributed to C–C (sp^2), defect peak (sp^3), C–O, C=O, and shakeup π–π^* satellite, respectively [32]. It is obvious that the content of C–O and C=O groups is far less than that of defect peak. To our best knowledge, the defect sp^3 carbon atoms and basal-plane sp^2 carbon atoms are two types of carbon atoms in different carbon materials. Hence, it is reasonable to infer the defect degree of carbon materials by evaluating the sp^2/sp^3 ratio. Compared to pristine CB (Fig. S4 in the ESM), the ratio of sp^2/sp^3 decreases from 7.125 to 6.625, 6.375, and 6.750 for CB-1, CB-2, and CB-3, suggesting the different defect degrees of these carbon materials, which is in good agreement with our Raman spectra result.

Meanwhile, the defective feature of CB samples was further detected by electron paramagnetic resonance (EPR). As exhibited in Fig. 2, the intensification of EPR signal along with the raising of H_2O_2 usage manifests the increase of defect degree of CB samples. Of particular note, CB-2 shows the EPR signal with the highest intensity because of more free electrons generated by more intrinsic deficiencies [33]. Moreover, the electron energy loss spectra (EELS) for CB and CB-2 were collected (Fig. S5 in the ESM). The carbon K-edge spectra of CB and CB-2 exhibit two main peaks at 285.5 and 292.8 eV, which are assigned to C=C π^* and C–C σ^* transitions in the hexagonal graphite layers. It is obvious that the intensified peak for CB-2 at 285.5 eV indicates an increase of carbon defects, which is consistent with the results from Raman, XPS, and EPR. All these characterization results demonstrate that the rich defects have been successfully introduced into carbon black material by our rationally regulated wet-chemistry defect engineering. Based on previous report [34], the possible defect forms are monovacancy graphene or divacancy graphene (Fig. S6 in the ESM). The existence of rich defects on carbon black has great potential to enhance the electrocatalytic activity of CB targeted promoted sulfur redox reaction kinetics.

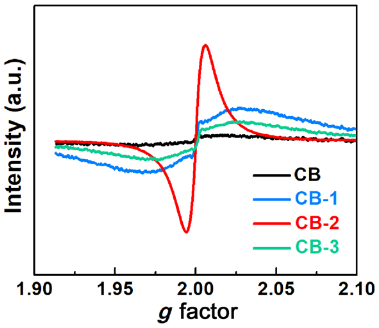

Figure 2 EPR spectra of CB, CB-1, CB-2, and CB-3.

To clearly confirm the restraining effect of defect engineering, visual LiPS adsorption tests were firstly conducted to probe the chemical interaction. As shown in Fig. S7 in the ESM, a certain amount of sample (10 mg) were added into Li_2S_4 solution. It is clearly observed that CB-2 decolored the Li_2S_4 solution after 1.0 h and completely fade into colorless solution after 5 h, manifesting its high adsorption efficiency towards LiPSs. Additionally, theoretical simulations by employing DFT calculation were conducted to verify the interaction between defect-rich carbon black and sulfur species based on possible existent forms in Fig. 3 and Fig. S6 in the ESM. Figures 3(a)–3(c) reveal that the adsorption energy values of monovacancy graphene and divacancy graphene towards Li_2S_4 are –0.673 and –1.065 eV, respectively, which are higher than that of graphene (–0.356 eV). Therefore, such strong Li_2S_4 adsorption ability of CB-2 not only is beneficial to alleviating shuttle effect but also offering abundant precursor source for LiPS conversion reaction. According to the Li_2S nucleation mechanism, the strong interfacial interaction between Li_2S and substrates is favorable for the nucleation reaction. As shown in Figs. 3(d)–3(f), the monovacancy graphene and divacancy graphene also show Li_2S adsorption energy values of –0.759 and –1.291 eV, which are higher than that of graphene (–0.487 eV), further substantiating the higher electrocatalytic activity of CB-2.

The electrocatalytic functions of various CB samples were further explored by a series of electrochemical characterizations. The discharge–charge profiles of S/CB, S/CB-1, S/CB-2, and S/CB-3 cathodes were compared. Figure 4(a) shows the partial part of the second discharge plateau which corresponds to the conversion of soluble Li_2S_4 to final insoluble Li_2S_2/Li_2S. S/CB-2 cathode exhibits the highest negative potential, suggesting the lowest overpotential. In addition, it can also be found that the capacity of S/CB-2 cathode at the negative potential is larger than those of other cathodes, implying its more outstanding effect on inhibiting LiPS shuttle. Likewise, the first part of the charge curve of S/CB-2 displays the lowest overpotential for the conversion of insoluble Li_2S_2/Li_2S to soluble LiPSs (Fig. 4(b)). Moreover, Li_2S nucleation tests were also carried out to explore the Li_2S nucleation kinetics by potentiostatically discharging Li_2S_8/tetraglyme solution at 2.05 V on various substrates, involving CB, CB-1, CB-2, and CB-3 loaded carbon papers (denoted as CP-CB, CP-CB-1, CP-CB-2, and CP-CB-3). As shown in Figs. 4(c)–4(f) and Fig. S8 in the ESM, the capacities

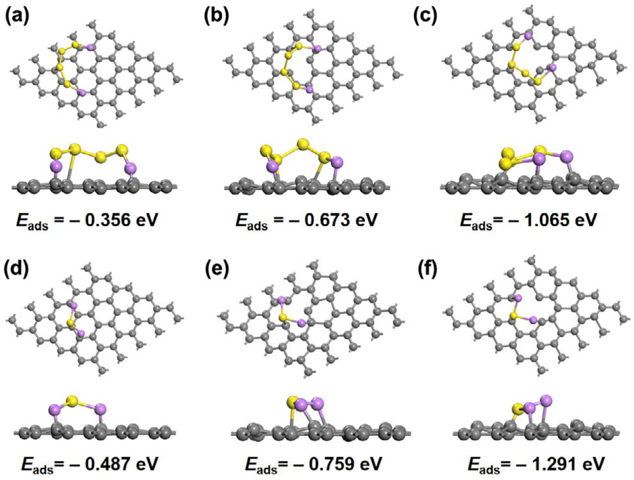

Figure 3 Binding configurations and related adsorption energies of (a)–(c) Li_2S_4 and (d)–(f) Li_2S on pristine grapheme ((a) and (d)), monovacancy graphene ((b) and (e)), and divacancy graphene ((c) and (f)).

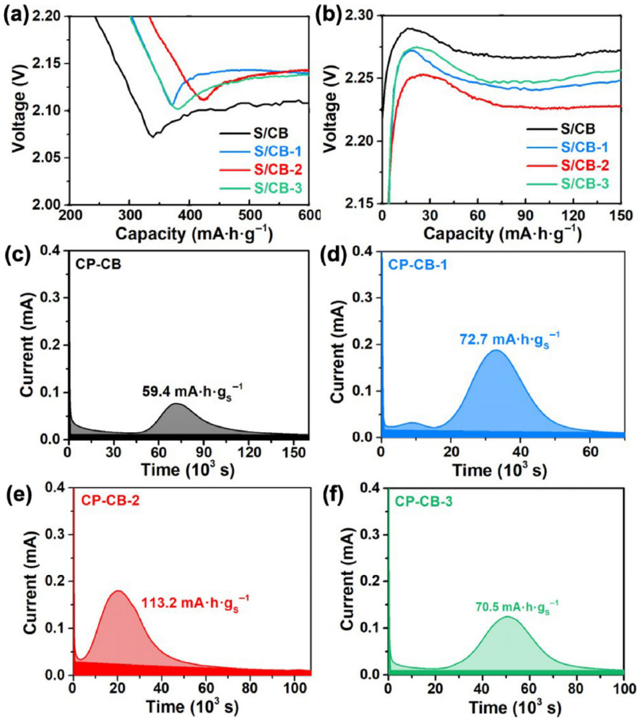

Figure 4 First cycle (a) discharge voltage and (b) charge voltage curves of S/CB, S/CB-1, S/CB-2, and S/CB-3 cathodes. (c)–(f) Potentiostatic discharge profiles of Li_2S_8/tetraglyme solution on CP-CB, CP-CB-1, CP-CB-2, and CP-CB-3 at 2.05 V.

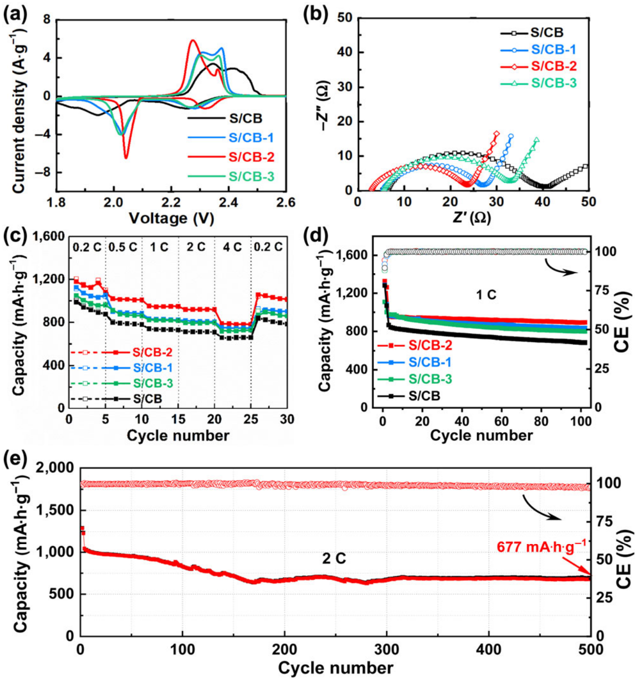

Figure 5 (a) CV curves, (b) EIS profiles, (c) rate capacities, and (d) cycling stability at 1 C of S/CB, S/CB-1, S/CB-2, and S/CB-3 cathodes. (e) Long-term cycling performance of S/CB-2 cathode at 2 C.

of Li_2S deposition on the surface of CB, CB-1, CB-2, and CB-3 are 59.4, 72.7, 113.2, and 70.5 mA·h·g^{-1}, respectively, manifesting higher electrocatalytic activity of CB-2 in contrast with other CB samples. These results verify that the defect engineering of CB is beneficial to accelerating the sulfur redox reaction kinetics, while the high defect degree CB-2 exhibits the best consequence.

The electrochemical performances of sulfur cathodes with the introduction of CB, CB-1, CB-2, and CB-3 as sulfur hosts were systematically evaluated. The sulfur loading content in the whole cathode was ~ 60 wt.% according to our thermo gravimetric analysis (TGA) results (Fig. S9 in the ESM). Figure 5(a) shows the typical cyclic voltammetric (CV) curves of different cathodes within the range of 1.8–2.6 V at a scan rate of 0.1 mV·s^{-1}. A pair of characteristic cathodic peaks located at 2.3 and 2.0 V can be attributed to the multistep reduction of solid sulfur to liquid high-order Li_2S_x ($4 \le x \le 8$) phase transition and further transformation to final insoluble discharge products of Li_2S_2/Li_2S. Correspondingly, the two anodic peaks can be assigned to the reverse conversion of Li_2S_2/Li_2S to LiPSs and then to sulfur. Compared with S/CB cathode, the S/CB-1, S/CB-2, and S/CB-3 cathodes clearly depict positive shifts in the cathodic peaks and negative shifts in the anodic peaks, accompanying with increased peak intensity, suggesting the decreased polarization and accelerated LiPS redox reaction kinetics. Remarkably, S/CB-2 cathode exhibits the most increased onset potential for sulfur reduction and the most decreased value for Li_2S oxidation, indicating the smallest polarization ascribing to its higher catalytic activity. Moreover, the smallest semicircle of S/CB-2 cathode in the EIS also provides clear evidence to substantiate such kinetic promotion during Li–S redox process (Fig. 5(b)). The rate capacities and cycling stability of cathodes were further evaluated. Figure 5(c) shows the comparison between the rate capabilities of S/CB, S/CB-1, S/CB-2, and S/CB-3 cathodes at various rates from 0.2 stepwise to 4 C every 5 cycles. Obviously, the S/CB-2 cathode delivers superior rate capacities of 1,179.1, 1,017.4, 950.4, 916.9, and 783.8 mA·h·g^{-1} at rates of 0.2, 0.5, 1, 2, and 4 C, respectively. When the rate is recovered to 0.2 C, the capacity can return to a high capacity of 1,058.2 mA·h·g^{-1}. The long-term cycling performance was also tested at 1 and 2 C. As shown in Fig. 5(d), the S/CB-2 cathode presents a discharge capacity of 891.7 mA·h·g^{-1} with a capacity retention of 91.8% over 100 cycles at 1 C, which is higher than those of S/CB-1 (835 mA·h·g^{-1} with a capacity retention of 86.4%), S/CB-3 (800 mA·h·g^{-1} with a capacity retention of 81.9%), and S/CB (684.4 mA·h·g^{-1} with a capacity retention of 78.9%). As the current increases to 2 C, S/CB-2 cathode still delivers a capacity of 677 mA·h·g^{-1} and coulombic efficiency (CE) over 97.8% after 500 cycles with a low capacity decay of only 0.07% per cycle, suggesting a favorable long-term cycling stability (Fig. 5(e)). In consideration of the demand for real applications, S/CB-2 cathode with high sulfur loading of 3.3 mg·cm^{-2} was also constructed. As shown in Fig. S10(a) in the ESM, the high-loading cathode delivers an initial area capacity of 940 mA·h·g^{-1} at 0.1 C. When the current density is raised to 0.5 C, the typical two-plateau voltage profile can still be obtained (Fig. S10(b) in the ESM) and a high capacity of 680 mA·h·g^{-1} can still be maintained even after 100 cycles. These results further indicate the great potential of such defect engineering-derived CB-2 on the design of commercially viable Li–S batteries.

The key issues, mainly pertaining to LiPS shuttle and retarded sulfur redox kinetics have posed a fatal threat to the real application of Li–S batteries. In response, defect catalysis serves as an emerging research strategy for designing high-efficiency and long-life Li–S batteries [35]. In this regard, our large-area and defect-rich CB offers more active sites for high-efficiency confinement of LiPSs and dynamically propel their conversion reaction, which is favor for realizing the effective regulation of LiPSs and optimizing the Li–S systems (Fig. 6).

4 Conclusions

In summary, defective carbon black was prepared through a rationally controlled wet-chemistry route. Such a defect-rich

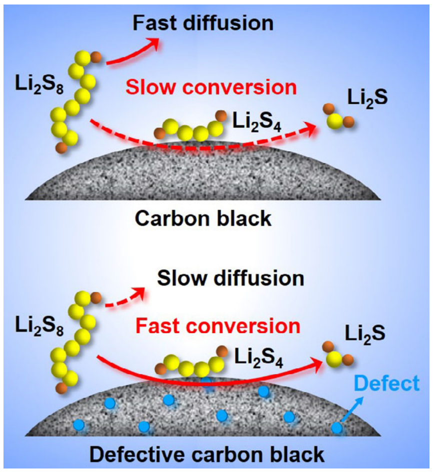

Figure 6 Schematic illustrating the role of defect-rich CB played in practical Li–S chemistry.

carbon black as sulfur host can decrease the overpotentials for LiPS transformation, accelerating the sulfur redox reaction kinetics, efficiently inhibiting the shuttle effect of LiPSs and thus enhancing the electrochemical performances of Li–S batteries. Our work would enable the fundamental understanding of underlying defect-catalytic mechanism and the practical design of high-performance Li–S battery systems.

Acknowledgements

This work was financially supported by the National Key Research and Development Program of China (No. 2017YFA0206703), the National Natural Science Foundation of China (No. 21671183), and the Project of State Key Laboratory of Environment-Friendly Energy Materials (SWUST, Nos. 19FKSY16 and 18ZD320304).

Electronic Supplementary Material: Supplementary material (SEM, N_2 adsorption–desorption measurements, XPS, EELS spectra, visualized adsorption tests, Li_2S nucleation tests, TGA curves, and electrochemical performance with high sulfur loading) is available in the online version of this article at https://doi.org/10.1007/s12274-020-3009-0.

References

[1] She, Z. W.; Sun, Y. M.; Zhang, Q. F.; Cui, Y. Designing high-energy lithium–sulfur batteries. *Chem. Soc. Rev*. **2016**, *45*, 5605–5634.

[2] Ousmane, I. A. M.; Li, R.; Wang, C.; Li, G. R.; Cai, W. L.; Liu, B. H.; Li, Z. P. Fabrication of oriented-macroporous-carbon incorporated with γ-Al_2O_3 for high performance lithium–sulfur battery. *Microporous Mesoporous Mater*. **2018**, *266*, 276–282.

[3] Yuan, H.; Peng, H. J.; Li, B. Q.; Xie, J.; Kong, L.; Zhao, M.; Chen, X.; Huang, J. Q.; Zhang, Q. Conductive and catalytic triple-phase interfaces enabling uniform nucleation in high-rate lithium–sulfur batteries. *Adv. Energy Mater*. **2019**, *9*, 1802768.

[4] Bhargav, A.; He, J. R.; Gupta, A.; Manthiram, A. Lithium–sulfur batteries: Attaining the critical metrics. *Joule* **2020**, *4*, 285–291.

[5] Ye, C.; Chao, D. L.; Shan, J. Q.; Li, H.; Davey, K.; Qiao, S. Z. Unveiling the advances of 2D materials for Li/Na–S batteries experimentally and theoretically. *Matter* **2020**, *2*, 323–244.

[6] Zhang, K. L.; Wang, L. B.; Cai, W. L.; Wang, C.; Li, G. R.; Li, Z. P.; Mao, W. T.; Qian, Y. T. A novel class of functional additives for cyclability enhancement of the sulfur cathode in lithium sulfur batteries. *Inorg. Chem. Front*. **2018**, *5*, 2013–2017.

[7] Song, Y. Z.; Sun, Z. T.; Fan, Z. D.; Cai, W. L.; Shao, Y. L.; Sheng, G.; Wang, M. L.; Song, L. X.; Liu, Z. F.; Zhang, Q. et al. Rational design of porous nitrogen-doped Ti_3C_2 MXene as a multifunctional electrocatalyst for Li–S chemistry. *Nano Energy* **2020**, *70*, 104555.

[8] Kong, L.; Jin, Q.; Zhang, X. T.; Li, B. Q.; Chen, J. X.; Zhu, W. C.; Huang, J. Q.; Zhang, Q. Towards full demonstration of high areal loading sulfur cathode in lithium–sulfur batteries. *J. Energy Chem*. **2019**, *39*, 17–22.

[9] Wang, S. Z.; Liao, J. X.; Yang, X. F.; Liang, J. N.; Sun, Q.; Liang, J. W.; Zhao, F. P.; Koo, A.; Kong, F. P.; Yao, Y. et al. Designing a highly efficient polysulfide conversion catalyst with paramontroseite for high-performance and long-life lithium–sulfur batteries. *Nano Energy* **2019**, *57*, 230–240.

[10] Chen, Y.; Zhang, W. X.; Zhou, D.; Tian, H. J.; Su, D. W.; Wang, C. Y.; Stockdale, D.; Kang, F. Y.; Li, B. H.; Wang, G. X. Co–Fe mixed metal phosphide nanocubes with highly interconnected-pore architecture as an efficient polysulfide mediator for lithium–sulfur batteries. *ACS Nano* **2019**, *13*, 4731–4741.

[11] Li, B. Q.; Kong, L.; Zhao, C. X.; Jin, Q.; Chen, X.; Peng, H. J.; Qin, J. L.; Chen, J. X.; Yuan, H.; Zhang, Q. et al. Expediting redox kinetics of sulfur species by atomic-scale electrocatalysts in lithium–sulfur batteries. *InfoMat* **2019**, *1*, 533–541.

[12] Chen, X.; Hou, T. Z.; Li, B.; Yan, C.; Zhu, L.; Guan, C.; Cheng, X. B.; Peng, H. J.; Huang, J. Q.; Zhang, Q. Towards stable lithium–sulfur batteries: Mechanistic insights into electrolyte decomposition on lithium metal anode. *Energy Storage Mater*. **2017**, *8*, 194–201.

[13] Zhang, G.; Zhang, Z. W.; Peng, H. J.; Huang, J. Q.; Zhang, Q. A toolbox for lithium–sulfur battery research: Methods and protocols. *Small Methods* **2017**, *1* 1700134.

[14] Yu, Z.; Zhang, J. J.; Wang, C.; Hu, R. X.; Du, X. F.; Tang, B.; Qu, H. T.; Wu, H.; Liu, X.; Zhou, X. H. et al. Flame-retardant concentrated electrolyte enabling a LiF-rich solid electrolyte interface to improve cycle performance of wide-temperature lithium–sulfur batteries. *J. Energy Chem*. **2020**, *51*, 154–160.

[15] Li, Z. H.; He, Q.; Xu, X.; Zhao, Y.; Liu, X. W.; Zhou, C.; Ai, D.; Xia, L. X.; Mai, L. Q. 3D nitrogen-doped graphene/tin nanowires composite as a strong polysulfide anchor for lithium–sulfur batteries with enhanced rate performance and high areal capacity. *Adv. Mater*. **2018**, *30*, 1804089.

[16] Ye, C.; Jiao, Y.; Jin, H. Y.; Slattery, A. D.; Davey, K.; Wang, H. H; Qiao, S. Z. 2D MoN-VN heterostructure to regulate polysulfides for highly efficient lithium–sulfur batteries. *Angew. Chem., Int. Ed*. **2018**, *57*, 16703–16707.

[17] Ye, Z. Q.; Jiang, Y.; Feng, T.; Wang, Z. H.; Li, L.; Wu, F.; Chen, R. J. Curbing polysulfide shuttling by synergistic engineering layer composed of supported Sn_4P_3 nanodots electrocatalyst in lithium–sulfur batteries. *Nano Energy* **2020**, *70*, 104532.

[18] Li, H. Y.; Fei, L. F.; Zhang, R.; Yu, S. L.; Zhang, Y. Y.; Shu, L. L.; Li, Y.; Wang, Y. FeCo alloy catalysts promoting polysulfide conversion for advanced lithium–sulfur batteries. *J. Energy Chem*. **2020**, *49*, 339–347.

[19] Li, G. R.; Cai, W. L.; Liu, B. H.; Li, Z. P. A multi functional binder with lithium ion conductive polymer and polysulfide absorbents to improve cycleability of lithium–sulfur batteries. *J. Power Sources* **2015**, *294*, 187–192.

[20] Huang, J. Q.; Liu, X. F.; Zhang, Q.; Chen, C. M.; Zhao, M. Q.; Zhang, S. M.; Zhu, W. C.; Qian, W. Z.; Wei, F. Entrapment of sulfur in hierarchical porous graphene for lithium–sulfur batteries with high rate performance from −40 to 60 °C. *Nano Energy* **2013**, *2*, 314–321.

[21] Xin, S.; Gu, L.; Zhao, N. H.; Yin, Y. X.; Zhou, L. J.; Guo, Y. G.; Wan, L. J. Smaller sulfur molecules promise better lithium–sulfur batteries. *J. Am. Chem. Soc*. **2012**, *134*, 18510–18513.

[22] Song, J. X.; Xu, T.; Gordin, M. L.; Zhu, P. Y.; Lv, D. P.; Jiang, Y. B.; Chen, Y. S.; Duan, Y. H.; Wang, D. H. Nitrogen-doped mesoporous carbon promoted chemical adsorption of sulfur and fabrication of high-areal-capacity sulfur cathode with exceptional cycling stability for lithium–sulfur batteries. *Adv. Funct. Mater*. **2014**, *24*, 1243–1250.

[23] Li, Q. C.; Song, Y. Z.; Xu, R. Z.; Zhang, L.; Gao, J.; Xia, Z.; Tian, Z. N.; Wei, N.; Rümmeli, M. H.; Zou, X. L. et al. Biotemplating growth of nepenthes-like n-doped graphene as a bifunctional polysulfide scavenger for Li−S batteries. *ACS Nano* **2018**, *12*, 10240–10250.

[24] Wang, Y. Z.; Adekoya, D.; Sun, J. Q.; Tang, T. Y.; Qiu, H. L.; Xu, L.; Zhang, S. Q.; Hou, Y. L. Manipulation of edge-site Fe-N_2 moiety on holey Fe, N codoped graphene to promote the cycle stability and rate capacity of Li–S batteries. *Adv. Funct. Mater*. **2018**, *29*, 1807485.

[25] Jia, Y.; Chen, J.; Yao, X. D. Defect electrocatalytic mechanism: Concept, topological structure and perspective. *Mater. Chem. Front.* **2018**, *2*, 1250–1268.

[26] Wang, W.; Shang, L., Chang, G. J.; Yan, C. Y.; Shi, R.; Zhao, Y. X.; Waterhouse, G. I. N.; Yang, D. J.; Zhang, T. R. Intrinsic carbon-defect-driven electrocatalytic reduction of carbon dioxide. *Adv. Mater.* **2019**, *31*, 1808276.

[27] Shen, A. L.; Zou, Y. Q.; Wang, Q.; Dryfe, R. A. W.; Huang, X. B.; Dou, S.; Dai, L. M.; Wang, S. Y. Oxygen reduction reaction in a droplet on graphite: Direct evidence that the edge is more active than the basal plane. *Angew. Chem., Int. Ed.* **2014**, *53*, 10804–10808.

[28] Kresse, G.; Joubert, D. From ultrasoft pseudopotentials to the projector augmented-wave method. *Phys. Rev. B* **1999**, 59, 1758–1775.

[29] Perdew, J. P.; Burke, K.; Ernzerhof, M. Generalized gradient approximation made simple. *Phys. Rev. Lett.* **1996**, 77, 3865–3868.

[30] Yu, J.; Wang, Y. L.; Zhao, C. F.; Chen, S. M.; Zhang, S. J. A 3D molecular cantilever based on interfacial self-assembly and the cobra-like actuation of long-chain imidazolium ionic liquids. *Nanoscale* **2019**, *11*, 7277–7286.

[31] Cai, W. L.; Li, G. R.; Zhang, K. L.; Zhou, J. B.; Qian, Y. T.; Du, J. A scalable *in situ* surfactant-free synthesis of a uniform MnO/graphene composite for highly reversible lithium storage. *Dalton Trans.* **2016**, *45*, 19221–19225.

[32] Tao, L.; Wang, Q.; Dou, S.; Ma, Z. L.; Huo, J.; Wang, S. Y.; Dai, L. M. Edge-rich and dopant-free graphene as a highly efficient metal-free electrocatalyst for the oxygen reduction reaction. *Chem. Commun.* **2016**, *52*, 2764–2767.

[33] Zhao, Y. Y.; Cai, W. L.; Fang, Y. T.; Ao, H. S.; Zhu, Y. C.; Qian, Y. T. Sulfur-deficient TiS_{2-x} for promoted polysulfide redox conversion in lithium–sulfur batteries. *ChemElectroChem* **2019**, *6*, 2231–2237.

[34] Liu, J.; Jiao, M. G.; Mei, B. B.; Tong, Y. X.; Li, Y. P.; Ruan, M. B.; Song, P.; Sun, G. Q.; Jiang, L. H.; Wang, Y. et al. Carbon-supported divacancy-anchored platinum single-atom electrocatalysts with superhigh Pt utilization for the oxygen reduction reaction. *Angew. Chem.* **2019**, *131*, 1175–1179.

[35] Zhang, Y. Q.; Tao, L.; Xie, C.; Wang, D. D.; Zou, Y. Q.; Chen, R.; Wang, Y. Y.; Jia, C. K.; Wang, S. Y. Defect engineering on electrode materials for rechargeable batteries. *Adv. Mater.* **2020**, *32*, 1905923.